J. Mech. Phys. Solids 182 (2024) 105462

Contents lists available at ScienceDirect

Journal of the Mechanics and Physics of Solids

journal homepage: www.elsevier.com/locate/jmps

Non-Hermitian wave dynamics of odd plates: Microstructure design and theoretical modelling

Yanzheng Wang, Qian Wu, Yiran Tian, Guoliang Huang *

Department of Mechanical and Aerospace Engineering, University of Missouri, Columbia, MO 65211, USA

ARTICLE INFO

Keywords:
2D non-Hermitian system
Odd elasticity
Active lattice plates
Interfacial waves
Nonreciprocal waves

ABSTRACT

The concept of odd elasticity was recently introduced to characterize the elastic behavior of solids that consist of active components, exhibiting an asymmetric elastic modulus tensor. In this paper, we propose, for the first time, the microstructure design of an odd plate, which is composed of a lattice plate with a piezoelectric-patch-based sensor–actuator feed-forward system. By leveraging the nonreciprocal coupling between shear forces and bending curvatures, the odd plate constitutive relation is formulated in the low frequency region, which features as four asymmetric coupling parameters known as "odd parameters". We reveal that the two-dimensional (2D) odd plates can perform directional wave energy amplification and the amplification angle can be determined analytically through the rotation of coordinate system. We also numerically demonstrate the directional wave amplification phenomena that arise from the optimal combination of odd parameters. In addition, we analytically uncover the presence of Stoneley-like interfacial waves between two plates with two odd parameters in opposite signs, which is further characterized by the numerical simulation. Unlike interfacial waves between topological structures, the interfacial waves between odd plates can exist for any working frequency, enabling the design of some novel waveguides. This research on the control of flexural waves in odd plates could shed lights on 2D non-Hermitian systems in elasticity.

1. Introduction

In the theory of linear elasticity, the conventional Cauchy medium with symmetry stiffness tensors has widely been accepted as the foundation of the continuum mechanics, however, the development of passive and active architecture metamaterials offers new avenues and perspectives to challenge and extend the fundamental basics. For example, introduction of chirality into mechanical metamaterials can break centrosymmetry of the mechanical behavior. In contrast with achiral mechanical metamaterials, chiral metamaterials exhibit nonzero force–torque coupling and are able to convert one transverse polarized elastic wave into the orthogonal transverse one, which cannot be captured by the conventional elasticity (Bahaloo and Li, 2019; Shaat and Park, 2023; Liu et al., 2012). Micropolar continuum mechanics under the Cosserat elasticity is then suggested by augmenting micro-rotation degrees of freedom to characterize the unconventional mechanical behavior (Nassar et al., 2020). Recently, the elastic polar solid was proposed as a perfect elastic wave cloaking material to possess elastic tensors with broken minor symmetry under frame of the Cauchy elasticity by introducing internal rotating resonators into hexachiral lattice (Nassar et al., 2019). However, most passive mechanical metamaterials designed to date are Hermitian systems with energy conservation such that their elastic constants describing the constitutive relations between stress and strain tensors under the higher-order theory are naturally symmetric such as Willis media (Milton and Willis, 2007), extreme media (Milton, 2013) and topological materials (Xue et al., 2022). The fundamental

* Corresponding author.
E-mail address: huangg@missouri.edu (G. Huang).

https://doi.org/10.1016/j.jmps.2023.105462
Received 11 July 2023; Received in revised form 12 September 2023; Accepted 6 October 2023
Available online 31 October 2023

limitation is that a passive solid cannot exchange energy from its surroundings through any quasistatic cycle of deformations, which will place additional constraints and freedoms to break symmetry of elastic moduli.

A growing frontier recently emerged on active metamaterials as non-Hermitian systems using external energy for various demands such as phononic gain, reconfigurability, or deterministic functionality (Wang et al., 2022; Rosa and Ruzzene, 2020; Gu et al., 2022; Zhang et al., 2022; Wu et al., 2023a; Brandenbourger et al., 2019; Yi et al., 2022; Wu et al., 2019; Domínguez-Rocha et al., 2020; Gupta et al., 2023). Non-Hermitian systems are generally defined as non-conservative systems where energy loss and/or gain are inherently present as a result of interactions with the environment that provides an energy source. Significant efforts have been made to interpret active systems featuring broken spatiotemporal symmetries, as well as violations of reciprocity relations and conservation laws. Formulating effective continuum theories of active metamaterial results in very general elastic constitutive relations, because in equilibrium such theories are not based on the elastic potential energy in active systems. Specifically, these active moduli could accommodate the antisymmetric (or odd) part of the static elastic modulus tensor giving rise to a loss of major symmetry, i.e., $C_{ijkl} = C_{klij}$, which is also termed as odd elasticity and odd elastodynamics (Scheibner et al., 2020b; Gao et al., 2022; Tan et al., 2022; Binysh and Souslov, 2022). From the mathematical point of view, the parity-time-reversal (PT) symmetry will be broken once the complex eigenvalues and non-orthogonal eigenmodes of the system appear, which are associated with exceptional points (El-Ganainy et al., 2018). The physical exploration of active microstructure designs is concurrently devoted to realizing peculiar material properties presenting non-Hermiticity outside of conventional media (Wu et al., 2023b). The active material displaying odd elasticity has been experimentally demonstrated by introducing piezoelectric elements and motors controlled by electrical circuits, or spinning networks, into host media (Chen et al., 2021; Brandenbourger et al., 2021). Additionally, these non-Hermitian systems with odd elasticity exhibit non-Hermitian one-dimensional (1D) and 2D skin effect and non-Hermitian Rayleigh wave propagation (Cheng and Hu, 2021; Gao et al., 2022; Scheibner et al., 2020a). Recently, active robotic materials were demonstrated to perform basic robotic manipulations such as steering motion and forces (Brandenbourger et al., 2021). Obviously, more feasible active microstructures are needed to explore more interesting non-Hermitian phenomena, especially the higher dimensional structures which allow more interesting wave controls and manipulations beyond the 1D system (Fruchart et al., 2023). It is thus intriguing to ask: how can we physically realize active bonds to form non-Hermitian mechanical 2D plates of odd elasticity? what is the unprecedented wave manipulation abilities in 2D active media which are never reported before? can interfacial waves exist in 2D non-Hermitian elastic system similar to their optical counterparts (Moccia et al., 2020)?

In this paper, we first aim to realize active microstructure design of a 2D non-Hermitian odd plate with feedforward interactions and explore a series of unconventional wave phenomena when conventional plate mechanics meets with non-Hermiticity. We report a type of active building blocks that contain an electrical control loop with multiple piezoelectric sensor–actuator-pairs. Assembling those active building blocks periodically constructs the 2D odd plate metamaterial with nonreciprocal coupling between bending moments and shear forces. The nonreciprocal wave amplification and attenuation phenomena and the direction-dependent dispersion control of flexural waves in the 2D odd plates are numerically shown. We analytically explain these phenomena and find that the metaplate breaks major symmetry of its effective elastic tensor, exhibiting odd plate. In addition, the equations describing the relation between the different odd coupling parameters are derived by the method of the rotation of coordinate system, by which the accurate control of the amplification-attenuation direction of flexural waves in odd plates can be realized. More interestingly, we also discover the localized interfacial wave modes between those finite odd plates. The existence of Stoneley-like interfacial waves is theoretically proved and numerically demonstrated between two odd plates with different odd parameters. We illustrate the underlying physical mechanisms and their intriguing properties, and also address possible practical implementations based on odd plates.

2. Microstructure design of an odd plate and its homogenization

The microstructure of the active odd plate is constructed by integrating piezoelectric sensors and actuators connected by a feed-forward circuit system with the host plate, which forms an open and non-Hermitian system. Fig. 1(a) illustrates the unit cell of an active lattice plate, consisting of a hollow plate with two crossing beams. Two slender piezoelectric patches are perpendicularly attached at the center on the top and bottom surfaces to serve as sensors and additional four piezoelectric patches are affixed on the four sides to act as actuators. The difference between a passive lattice and the present active lattice is the presence of internal energy sources (active beams in this study). The sensor is used to detect the incident wave by measuring the local bending curvature of the beam, and the actuators are employed to generate desired antisymmetric shear fields through the application of antisymmetric actuation voltages (Wu et al., 2022). Transfer functions are encoded in the digital controller and control relations between sensing and actuating signals of the active beams. However, the resulting shear deformation does not deform the central piezoelectric sensing patches. Therefore, the electromechanical control loop is entirely feedforward, which means bending induces shear, while shear does not induce bending. The schematic of digital control system is presented in Fig. A.1 in Appendix A. The material and unit cell geometric parameters are listed in Tables 1 and 2, respectively.

In the current design, it is challenging to measure the bending curvatures in the x- and y-directions separately using piezoelectric sensors. To overcome this limitation, a relationship between the two bending curvatures and the voltages collected from the top (V_T) and bottom (V_B) piezoelectric sensors is numerically constructed as

$$\begin{bmatrix} V_T \\ -V_B \end{bmatrix} = C_m \begin{bmatrix} 1 & \beta \\ \beta & 1 \end{bmatrix} \begin{bmatrix} B_x \\ B_y \end{bmatrix}, \tag{1}$$

where B_x and B_y denote the bending curvatures in the x- and y-directions, respectively, and C_m and β are constant to be numerically determined by using the COMSOL Multiphysics software. It should be pointed out that the top and bottom voltages

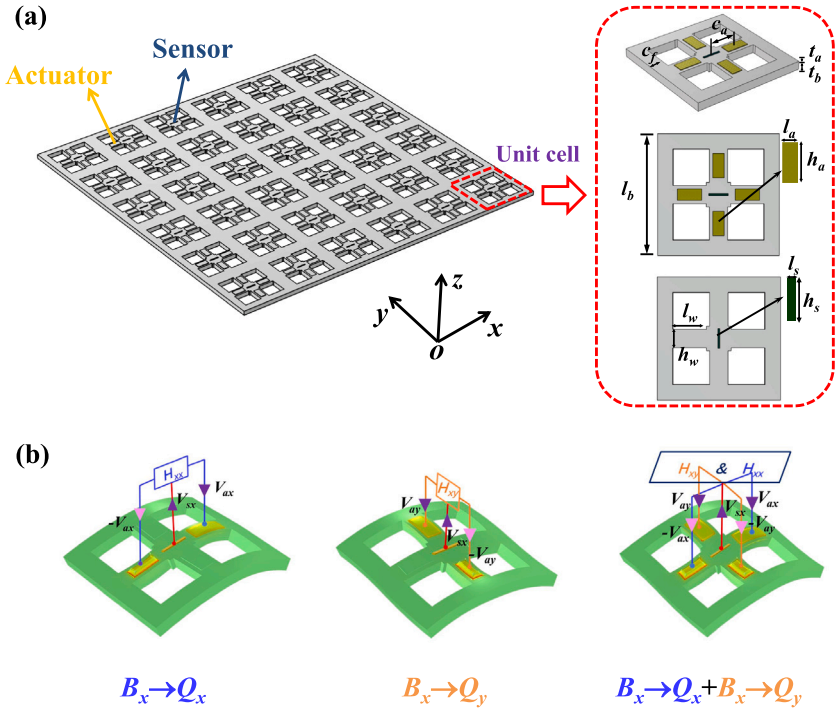

Fig. 1. Design of an active lattice plate with odd elasticity. (a) The lattice structure of the plate is composed of feed-forward systems involving sensor–actuator loops. The side, top, and front views of the lattice plate's unit cell are illustrated. (b) The piezoelectric-patch-based feed-forward control enables the coupling between the sensed x-directional bending deformation (B_x) and the actuated shear deformations (Q_x and/or Q_y) in different directions.

Table 1
Material parameters for steel and PZT-5J.

ρ_b	7800 kg/m^3	E	205 GPa	ν	0.3
ρ_p	7400 kg/m^3	s_{11}	1.62×10^{-12} Pa^{-1}	s_{12}	-4.54×10^{-12} Pa^{-1}
s_{13}	-5.9×10^{-12} Pa^{-1}	s_{33}	2.27×10^{-11} Pa^{-1}	s_{44}	4.7×10^{-11} Pa^{-1}
s_{66}	4.15×10^{-11} Pa^{-1}	d_{31}	-2.2×10^{-10} C/N	d_{33}	5×10^{-10} C/N
d_{15}	6.7×10^{-10} C/N	ϵ_{11}	1641.3	ϵ_{33}	1143

of the piezoelectric sensors are achieved via the detection of the corresponding electric charges with the relations $V_T = q_T/c_0$ and $V_B = q_B/c_0$, where q_T and q_B are the electric charges on the surfaces of the piezoelectric sensors, and c_0 is the reference capacitance, which is selected as 1.658 pF in this paper. Thus, the sensing voltages related to the bending curvatures in the x- and y-directions can be obtained as

$$V_{sx} = V_T + \beta V_B, \quad V_{sy} = -\beta V_T - V_B. \tag{2}$$

As seen schematically from Fig. 1(b), the connections between the actuating and sensing voltages are established through the microcontroller as

$$V_{ax} = H_{xx}V_{sx} + H_{yx}V_{sy}, V_{ay} = H_{xy}V_{sx} + H_{yy}V_{sy}, \tag{3}$$

where H_{xx}, H_{xy}, H_{yx}, and H_{yy} are the four transfer functions to be used. In this system, the antisymmetric actuation generates shear deformations either in one direction or two directions. Thus, the shear deformations can be nonreciprocally coupled with the bending deformation in the x- or y-direction. As a result, the relation between the shear forces and the bending curvatures in the active plate in Fig. 1 can be constructed as

$$Q_x = Q_x^s + P_{xx}B_x + P_{yx}B_y, \tag{4}$$

$$Q_y = Q_y^s + P_{xy}B_x + P_{yy}B_y, \tag{5}$$

where Q_x^s and Q_y^s are the shear forces on the sections in the x- and y-directions, respectively, induced by the shear deformations and P_{xx}, P_{xy}, P_{yx}, and P_{yy} are referred to as the parameters related to the transfer functions to be determined numerically. Physically, P_{xx} and P_{yy} represent the bending–shear couplings along the x and y directions, respectively, and P_{xy} and P_{yx} represent the bending–shear cross couplings between the x- and y-directions, respectively. It is worth noting that the value of each parameter can be independently tuned through the transfer functions, which is one of the primary advantages of the proposed design.

Table 2
Geometric parameters for the unit cell.

l_b	50 mm	t_b	3 mm	h_s	6.4 mm	l_s	0.64 mm
l_w	11 mm	h_w	6 mm	c_f	10 mm	l_a	3.75 mm
h_a	8 mm	t_a	0.25 mm	c_a	9.5 mm		

The homogenization of the active lattice plate will then be conducted under the framework of the Mindlin plate theory by assuming the displacement components as

$$u_x = z\psi_x(x,y,t), u_y = z\psi_y(x,y,t), u_z = w(x,y,t), \tag{6}$$

where w is the z-directional displacement, and ψ_x and ψ_y represent the rotation angles of the lines normal to the mid-planes in the x- and y-directions, respectively. The bending curvatures can then be represented by

$$B_x = \frac{\partial \psi_x}{\partial x}, B_y = \frac{\partial \psi_y}{\partial y}, B_{xy} = \frac{\partial \psi_y}{\partial x} + \frac{\partial \psi_x}{\partial y}, \tag{7}$$

and the shear strains are

$$\gamma_{xz} = \frac{\partial w}{\partial x} + \psi_x, \quad \gamma_{yz} = \frac{\partial w}{\partial y} + \psi_y. \tag{8}$$

The constitutive relation of the active plate can be obtained by combining Eqs. (4)–(8) as

$$\begin{pmatrix} M_x \\ M_y \\ M_{yx} \\ Q_x \\ Q_y \end{pmatrix} = \begin{pmatrix} D_{11} & D_{12} & 0 & 0 & 0 \\ D_{12} & D_{11} & 0 & 0 & 0 \\ 0 & 0 & D_{33} & 0 & 0 \\ P_{xx} & P_{yx} & 0 & G & 0 \\ P_{xy} & P_{yy} & 0 & 0 & G \end{pmatrix} \begin{pmatrix} B_x \\ B_y \\ B_{xy} \\ \gamma_{xz} \\ \gamma_{yz} \end{pmatrix}, \tag{9}$$

where D_{11}, D_{12} and D_{33} are the bending stiffnesses, and G is the shear stiffness. From Eq. (9), it is interesting to note that the stiffness matrix of the plate lose the major symmetry due to the asymmetric appearance of the active parameters in the off-diagonal entries (P_{xx}, P_{yy}, P_{xy} and P_{yx} being nonzero). The plate is referred to as the odd plate, and the active parameters are called the odd parameters in the following part. As a result, the work in the odd plate can be locally extracted, or injected, during the quasi-static cycles of plate deformation (Chen et al., 2021).

As a matter of fact, this novel electromechanical coupling in the odd plate is feed-forward: bending deformations cause shear forces while shear strains do not induce bending moments, which violates Maxwell–Betti reciprocity. In general, one should expect to observe the odd phenomenon when nonreciprocal shear and bending coupling exists. For instance, the stiffness matrix of the plate displays asymmetry in cases where shear induces bending, while bending alone does not induce shear. Odd wave phenomena such as asymmetric and nonreciprocal wave propagation are expected to occur. It is worth noting that the extent of these odd phenomena becomes more prominent with larger values of the odd parameters.

We then quantitatively retrieve the effective elastic tensor of the odd plate. The effective moduli in Eq. (9) can be obtained by applying strain-controlled boundary conditions at the terminating faces of a unit cell and analyzing the reaction forces via COMSOL simulations. The effective bending stiffness, shear stiffness and odd parameters can be determined separately under three different deformation modes of the plate: bending, shear, and twist modes. For instance, the harmonic rotational angles, ψ_x^0 and $-\psi_x^0$, are applied onto the two boundary surfaces in the x-direction. While the rotations of the other two boundary surfaces in the other directions are fixed, other displacement components are released to obtain the pure bending deformation in the x-direction. In this way, the effective parameters D_{11}, D_{12}, P_{xx} and P_{xy} can be calculated as $M_x^0/2\psi_x^0$, $M_y^0/2\psi_x^0$, $Q_x^0/2\psi_x^0$, and $Q_y^0/2\psi_x^0$, respectively, where M_x^0, M_y^0, Q_x^0, and Q_y^0 are the reaction bending moments and shear forces in the x- and y-directions, respectively. A similar methodology can be applied to determine the other effective parameters. The average volumetric density and average cross-sectional moment of inertia can be directly computed based on the geometry and materials of the unit cell.

Based on the odd constitutive relation in Eq. (9), the governing equations of the odd plate can be written as

$$\begin{aligned} G\left[\left(\frac{\partial^2}{\partial x^2} + \frac{\partial^2}{\partial y^2}\right)w + \frac{\partial^2 \psi_x}{\partial x} + \frac{\partial^2 \psi_y}{\partial y}\right] &+ P_{xx}\frac{\partial^2 \psi_x}{\partial x^2} + \frac{\partial^2}{\partial x \partial y}\left(P_{yx}\psi_y + P_{xy}\psi_x\right) \\ &+ P_{yy}\frac{\partial^2 \psi_y}{\partial y^2} = \rho h \frac{\partial^2 w}{\partial t^2}, \end{aligned} \tag{10}$$

$$\begin{aligned} D_{11}\frac{\partial^2 \psi_x}{\partial x^2} + D_{33}\frac{\partial^2 \psi_x}{\partial y^2} + \left(D_{12} + D_{33}\right)\frac{\partial^2 \psi_y}{\partial x \partial y} &- G\left(\frac{\partial w}{\partial x} + \psi_x\right) - P_{xx}\frac{\partial \psi_x}{\partial x} \\ &- P_{yx}\frac{\partial \psi_y}{\partial y} = \frac{\rho h^3}{12}\frac{\partial^2 \psi_x}{\partial t^2}, \end{aligned} \tag{11}$$

$$\begin{aligned} D_{33}\frac{\partial^2 \psi_y}{\partial x^2} + D_{11}\frac{\partial^2 \psi_y}{\partial y^2} + \left(D_{12} + D_{33}\right)\frac{\partial^2 \psi_x}{\partial x \partial y} &- G\left(\frac{\partial w}{\partial y} + \psi_y\right) - P_{xy}\frac{\partial \psi_x}{\partial x} \\ &- P_{yy}\frac{\partial \psi_y}{\partial y} = \frac{\rho h^3}{12}\frac{\partial^2 \psi_y}{\partial t^2}. \end{aligned} \tag{12}$$

where ρ and h are the mass density and the thickness of the plate, respectively. We assume the time-harmonic wave solutions as

$$w = W e^{i(\mathbf{k}\cdot\mathbf{r} - \omega t)}, \quad \psi_x = \Psi_x e^{i(\mathbf{k}\cdot\mathbf{r} - \omega t)}, \quad \psi_y = \Psi_y e^{i(\mathbf{k}\cdot\mathbf{r} - \omega t)}, \tag{13}$$

where $\mathbf{k} = k_x\mathbf{e}_x + k_y\mathbf{e}_y$, $\mathbf{r} = x\mathbf{e}_x + y\mathbf{e}_y$, $\mathbf{e}_x$ and $\mathbf{e}_y$ are the base vectors in the x- and y-directions, respectively. The components of the wave vector is given by $k_x = |\mathbf{k}|\cos\theta$ and $k_y = |\mathbf{k}|\sin\theta$, with θ indicating the wave propagation direction. Substituting Eq. (13) into Eqs. (10)–(12), the governing equations for flexural waves can be recast into a dimensionless matrix form as

$$\begin{pmatrix} c_{11} & c_{12} & c_{13} \\ c_{21} & c_{22} & c_{23} \\ c_{31} & c_{32} & c_{33} \end{pmatrix} \begin{pmatrix} \bar{W} \\ \Psi_x \\ \Psi_y \end{pmatrix} = \begin{pmatrix} 0 \\ 0 \\ 0 \end{pmatrix}, \tag{14}$$

where

$$\begin{aligned}
&c_{11} = \Omega^2 - \left(\bar{k}_y^2 + \bar{k}_x^2\right), \quad c_{12} = i\bar{k}_x - \bar{P}_{xx}\bar{k}_x^2 - \bar{P}_{xy}\bar{k}_x\bar{k}_y, \\
&c_{13} = i\bar{k}_y - \bar{P}_{yx}\bar{k}_x\bar{k}_y - \bar{P}_{yy}\bar{k}_y^2, \quad c_{21} = -i\bar{k}_x, \\
&c_{22} = \frac{\Omega^2}{12} - \bar{D}_{11}\bar{k}_x^2 - \bar{D}_{33}\bar{k}_y^2 - 1 - i\bar{P}_{xx}\bar{k}_x, \\
&c_{23} = -\left[\left(\bar{D}_{12} + \bar{D}_{33}\right)\bar{k}_x\bar{k}_y + i\bar{P}_{yx}\bar{k}_y\right], \\
&c_{31} = -i\bar{k}_y, \quad c_{32} = -\left[\left(\bar{D}_{12} + \bar{D}_{33}\right)\bar{k}_x\bar{k}_y + i\bar{P}_{xy}\bar{k}_x\right], \\
&c_{33} = \frac{\Omega^2}{12} - \bar{D}_{33}\bar{k}_x^2 - \bar{D}_{11}\bar{k}_y^2 - 1 - i\bar{P}_{yy}\bar{k}_y.
\end{aligned}$$

The above dimensionless quantities are defined as

$$\begin{aligned}
&\Omega^2 = \frac{\rho\omega^2 h^3}{G}, \quad \bar{k}_x = k_x h, \quad \bar{k}_y = k_y h, \quad \bar{P}_{xx} = \frac{P_{xx}}{Gh}, \quad \bar{P}_{yy} = \frac{P_{yy}}{Gh}, \\
&\bar{P}_{xy} = \frac{P_{xy}}{Gh}, \quad \bar{P}_{yx} = \frac{P_{yx}}{Gh}, \quad \bar{D}_{11} = \frac{D_{11}}{Gh^2}, \quad \bar{D}_{12} = \frac{D_{12}}{Gh^2}, \quad \bar{D}_{33} = \frac{D_{33}}{Gh^2}.
\end{aligned}$$

To obtain the nontrivial solutions to Eq. (14), the matrix determinant should be zero:

$$\begin{vmatrix} c_{11} & c_{12} & c_{13} \\ c_{21} & c_{22} & c_{23} \\ c_{31} & c_{32} & c_{33} \end{vmatrix} = 0. \tag{15}$$

The dispersion relation for flexural waves propagating in the odd plate can be obtained by solving Eq. (15).

The dispersion relation for the flexural waves propagating in the active lattice, as depicted in Fig. 1, can be obtained by applying the periodic boundary conditions to the corresponding unit cell. The comparison of the equi-frequency contours for the real parts of eigenfrequencies are shown in Fig. 2(a) and (c), and the comparisons for the corresponding imaginary parts are shown in Fig. 2(b) and (d). Two types of unit cells are considered, differing only in their transfer functions or odd parameters. In Fig. 2(a) and (b), the nonzero odd parameters are $\bar{P}_{xx} = \bar{P}_{yy} = 1.96$ for the nonzero transfer functions $H_{xx} = H_{yy} = 6$, while in Fig. 2(c) and (d), they read $\bar{P}_{xy} = 1.96$ for $H_{xy} = 6$. The remaining plate moduli are calculated as $\rho_{\text{eff}} = 6046.93$ kg/m^3, $G = 1.68 \times 10^6$ N/m, $D_{11} = 291.28$ N m, $D_{12} = 51.60$ N m, $D_{33} = 121.96$ N m, and $\beta = 0.28$.

It should be noted that the comparisons of the equi-frequency contours for the real parts of eigenfrequencies in Fig. 2(a) and (c) exhibit excellent agreements, while some discrepancies are observed in Fig. 2(b) and (d) through the comparisons of the contours for the corresponding imaginary parts, which is caused by the nonreciprocal coupling between bending deformation and shear stress in the active lattice. To further understand the reason for these discrepancies, the shear deformation fields caused by the active beams within the unit cell are illustrated in Fig. B.1 in Appendix B. It is clearly evidenced that the distribution of actively applied shear stresses is non-uniform and predominantly concentrated at the positions of the active beams even for the static case. The uneven active stresses are responsible for the discrepancies of the imaginary parts of eigenfrequencies between the active lattice and the effective plate in Fig. 2(b) and (d). In particular, in the scenario depicted in Fig. 2(d), where there is just one active beam in the y-direction, the discrepancies remain relatively minor when the wave travels in a direction close to the y-axis. These discrepancies grow as the wave propagation deviates from this direction. However, the discrepancies around the x-axis are not obvious since the magnitudes of the imaginary parts of eigenfrequencies are small around this direction. The reason behind this phenomenon is that the effects of the applied shear stresses on the waves propagating away from the y-direction become smaller. As a comparison, for the case of the unit cell with two orthogonal active beams in Fig. 2(b), the shear deformation caused by the two active beams is much more uniform. As a result, the discrepancy becomes relatively smaller for most wave directions close to both the x- and y-directions, compared with the case of one active beam. For this case, the biggest discrepancies occur at the angles 0.25π and 1.25π; see Fig. 2(b). It can be understood that the two orthogonal active beams have the smallest influences on the frame at the angles of 0.25π, 0.75π, 1.25π, and 1.75π. However, the discrepancies around the angles 0.75π and 1.75π are not obvious due to the small magnitudes of the imaginary parts of eigenfrequencies since the two active beams have the opposite influences around these two angles; see Fig. B.1(b). Ideally, the discrepancy can be totally eliminated if the interior active beams are uniformly distributed.

The active lattice plate can also be viewed as an equivalent homogeneous plate composed of orthotropic materials. The approximate values for the effective Young's modulus, shear stiffness, and Poisson's ratio are as follows: $E_1 = E_2 = 125.402$ GPa, $G_{12} = 54$ GPa, $G_{13} = G_{23} = 0.67$ GPa, and $\nu_{12} = 0.177$. Thus, the iso-frequency contours of the odd plates can also be obtained using the plate module in COMSOL Multiphysics, where the contribution from odd elasticity is accounted by using weak forms. Both the odd plate theory and COMSOL simulation will be employed to investigate the propagation of flexural waves and reveal novel wave phenomena in the subsequent analyses.

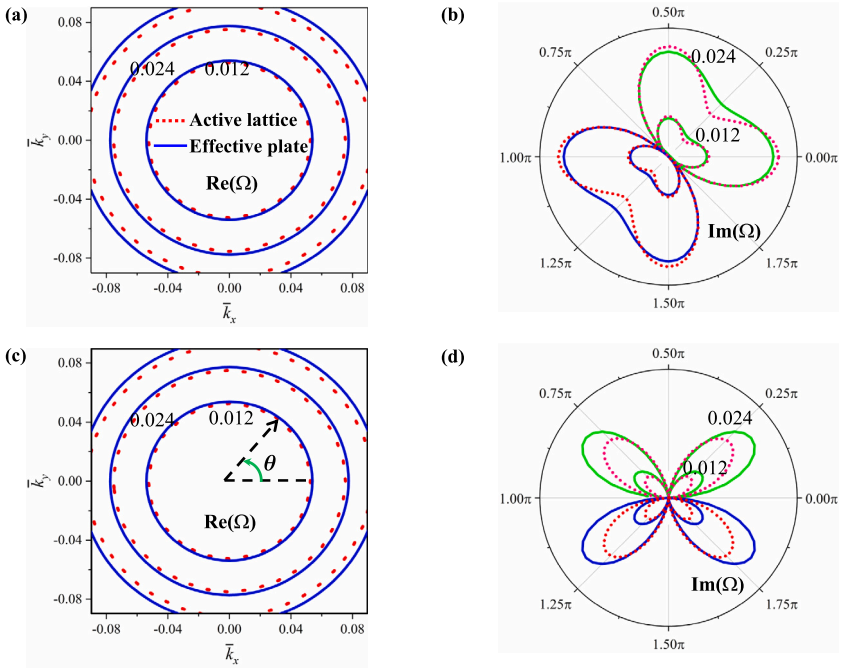

Fig. 2. Comparison of the iso-frequency contours of the active lattice plate with those of the effective odd plates. (a) Iso-frequency contours in terms of real parts of the eigenfrequencies with the nonzero odd parameters $\bar{P}_{xx} = \bar{P}_{yy} = 1.96$ and (b) the imaginary parts of eigenfrequencies for the specific real parts of the eigenfrequencies being 0.012 and 0.024. (c) Iso-frequency contours in terms of real parts of the eigenfrequencies with the nonzero odd parameters $\bar{P}_{xy} = 1.96$ and (d) the imaginary parts of eigenfrequencies for the specific real parts of the eigenfrequencies being 0.012 and 0.024. In these plots, the dotted lines represent the iso-frequency contours of the active lattice plates, which are obtained from COMSOL simulations, while the solid lines represent the iso-frequency contours of the effective odd plates calculated by using the homogenization theory. In (b) and (d), the radial coordinates denote the magnitudes of the imaginary parts of eigenfrequencies.

3. Flexural wave propagation in odd plates

The constitutive relation of an odd plate has been obtained from continuum point of view. In this section, the dynamic behavior such as flexural wave propagation is under consideration. Similarly, the harmonic flexural wave with complex wave vector in the odd plate is assumed as

$$w = W e^{-\mathbf{k}_I \cdot \mathbf{r}} e^{i(\mathbf{k}_r \cdot \mathbf{r} - \omega t)}, \quad \psi_x = \Psi_x e^{-\mathbf{k}_I \cdot \mathbf{r}} e^{i(\mathbf{k}_r \cdot \mathbf{r} - \omega t)}, \quad \psi_y = \Psi_y e^{-\mathbf{k}_I \cdot \mathbf{r}} e^{i(\mathbf{k}_r \cdot \mathbf{r} - \omega t)}, \tag{16}$$

where $\mathbf{k}_r$ and $\mathbf{k}_I$ denote the real and imaginary parts of the wave vector, respectively, to represent wave amplification or attenuation with $-\mathbf{k}_I \cdot \mathbf{r}$ being the amplitude amplification factor. This amplification or attenuation behavior depends on the projection of the imaginary part of the wave vector on the wave propagation direction.

To identify the odd parameter effects on the wave propagation, the iso-frequency contours in terms of real and imaginary parts of wave number is displayed in Fig. 3 for the dimensionless frequencies $\Omega = 0.03, 0.06, 0.09$ with only one nonzero odd parameter while the other three being zero such as case 1: $\bar{P}_{xx} = 1.96, \bar{P}_{yy} = \bar{P}_{xy} = \bar{P}_{yx} = 0$; case 2: $\bar{P}_{yx} = 1.96, \bar{P}_{xx} = \bar{P}_{yy} = \bar{P}_{xy} = 0$; case 3: $\bar{P}_{xy} = 1.96, \bar{P}_{xx} = \bar{P}_{yy} = \bar{P}_{yx} = 0$; and case 4: $\bar{P}_{yy} = 1.96, \bar{P}_{xx} = \bar{P}_{xy} = \bar{P}_{yx} = 0$, respectively. The real part in Fig. 3(a–d) represent isotropic flexural wave propagation, which closely resembles that of a passive 2D plate without control. Therefore, the variation of odd parameters has minimal influence on the real part of the wave number. The imaginary part of the frequency contours in Fig. 3(e–h) exhibits directional dependent attenuation and amplification zones at a specific frequency. For each case, the iso-frequency contour for the imaginary part of the wave number appears in only one direction. For waves propagating along the direction where the iso-frequency contour collects, they will be attenuated as the propagation distance increases. Conversely, when waves propagate along the opposite direction, they will be amplified. For example, Fig. 3(e) and (f) demonstrate that positive odd parameters P_{xx} and P_{yx} amplify waves along the negative direction of the x-axis and attenuate waves along the positive direction of the x-axis. On the other hand, positive odd parameters P_{xy} and P_{yy} amplify waves along the negative direction of the y-axis and attenuate waves along the positive direction of the y-axis, as shown in Fig. 3(g) and (h). It is important to note that the amplification and attenuation directions would exchange when the odd parameters become negative, although this is not presented in the paper. When comparing the magnitudes of the imaginary parts of wave numbers in Fig. 3(e–h) for the four different odd parameters, we find that odd parameters P_{xx} and P_{yy} lead to larger imaginary parts of wave numbers, while the imaginary parts of wave numbers corresponding to P_{xy} and P_{yx} are smaller. This implies that the same directional bending–shear coupling results in a larger wave amplification or attenuation. The numerical simulation results shown in Fig. 3(i–l) further support the amplification-attenuation

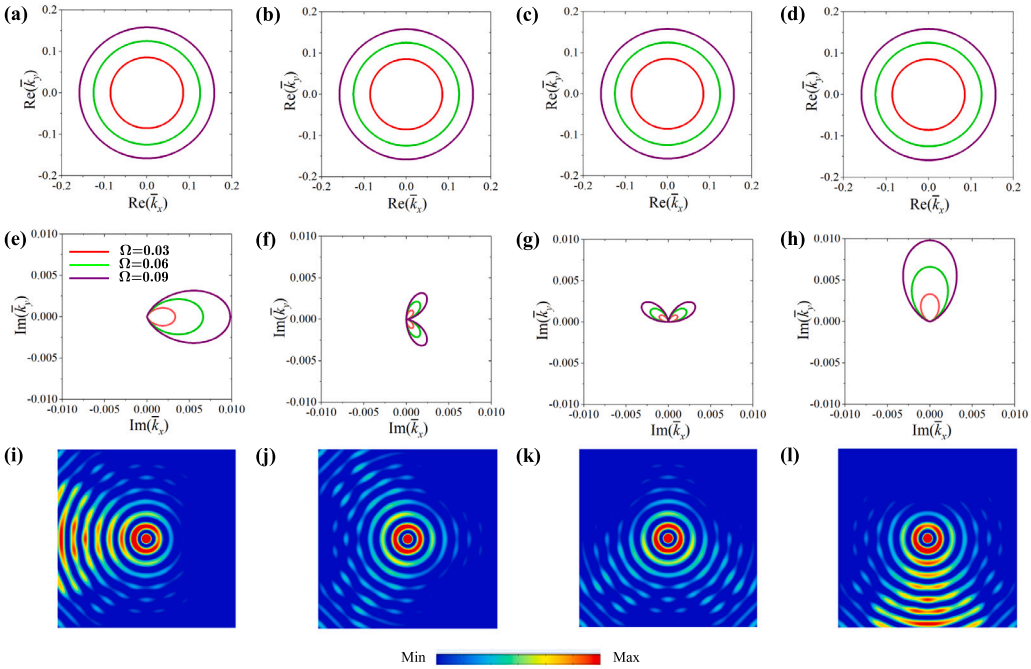

Fig. 3. Influence of each odd parameter on directional flexural wave propagation. (a–d) Iso-frequency contours as functions of real part of wave number. (e–h) Iso-frequency contours as functions of imaginary part of wave number. (i–l) Corresponding simulations for directional flexural wave propagation in the considered scenarios. Starting from the left side, the figures in the first to fourth columns correspond to: case 1 ($\bar{P}_{xx} = 1.96, \bar{P}_{yy} = \bar{P}_{xy} = \bar{P}_{yx} = 0$); case 2 ($\bar{P}_{yx} = 1.96, \bar{P}_{xx} = \bar{P}_{yy} = \bar{P}_{xy} = 0$); case 3 ($\bar{P}_{xy} = 1.96, \bar{P}_{xx} = \bar{P}_{yy} = \bar{P}_{yx} = 0$); and case 4 ($\bar{P}_{yy} = 1.96, \bar{P}_{xx} = \bar{P}_{xy} = \bar{P}_{yx} = 0$).

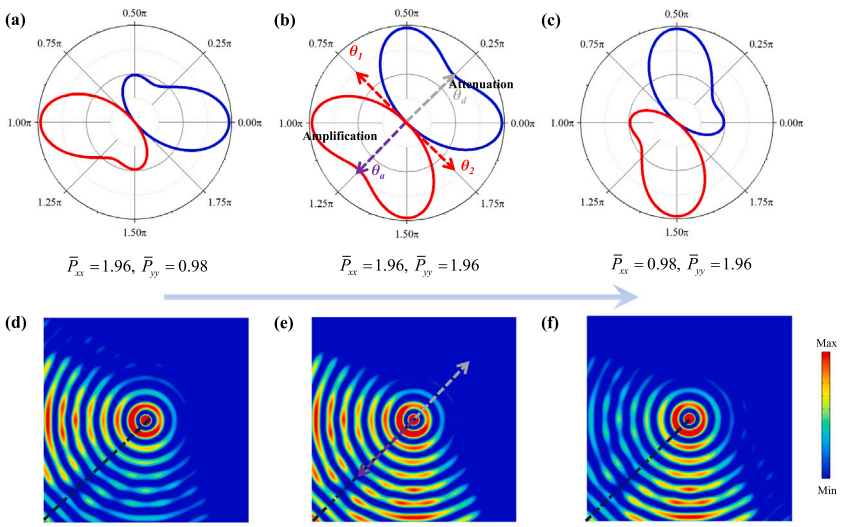

Fig. 4. Tunability of the wave amplification direction in the odd plate with bending–shear couplings in the same direction, i.e., $\bar{P}_{xx} = \bar{P}_{yy} \neq 0$ but $\bar{P}_{xy} = \bar{P}_{yx} = 0$. (a–c) Iso-frequency contours in terms of imaginary parts of wave number. (d–f) Corresponding simulations for directional flexural wave propagation in the considered scenarios. The red contours represent wave amplification profiles, while the blue contours represent wave attenuation profiles.

directions of flexural waves for the four different cases. In the simulation, damping boundaries are implemented to serve as perfect matched layers (PMLs) in all simulations of flexural waves propagating in odd plates for $\Omega = 0.03$.

It is of interest here to explore how the odd parameters control the flexural wave amplification directions in odd plates. One simple approach to accomplish this goal is to adjust the magnitudes of the two odd parameters, $\bar{P}_{xx}$ and $\bar{P}_{yy}$. Fig. 4 plots the iso-frequency contours for the imaginary parts of the wave numbers in polar coordinate systems for adjusting the ratio of two nonzero odd parameters. It is clearly demonstrated that the wave amplification direction can be shifted by just adjusting the ratio of the

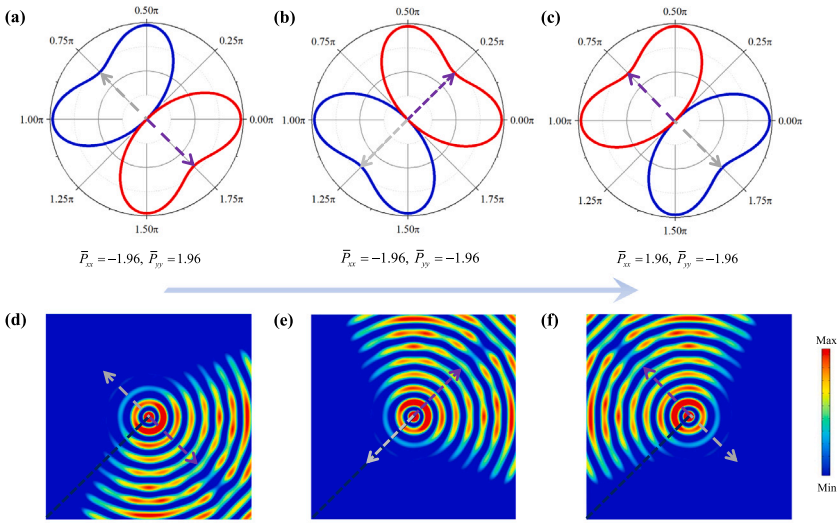

Fig. 5. Control of the amplification directions for flexural waves by changing the signs of the odd parameters $\bar{P}_{xx}$ and $\bar{P}_{yy}$ with $\bar{P}_{xy} = \bar{P}_{yx} = 0$. (a–c) The iso-frequency contours for the imaginary parts of wave number for $\theta_a = 1.75\ \pi$, $0.25\ \pi$, and $0.75\ \pi$, (d–f) Corresponding simulations for directional amplification of flexural waves in the considered scenarios.

two odd parameters, $\bar{P}_{xx}/\bar{P}_{yy}$. Also, we observe that waves propagating close to the directions with larger odd parameters undergo stronger amplification.

To further characterize the wave amplification, we introduce θ_a and θ_d, which represent the central angles of the amplification and the attenuation profiles, respectively. These angles are indicated by the purple and the gray dotted arrow lines in Fig. 4(b), and the profiles are evenly distributed on both sides of the two lines. Mathematically, the two central angles can be defined as

$$\theta_a = \frac{\theta_1 + \theta_2}{2}, \theta_d = \theta_a - \pi, \tag{17}$$

where θ_1 and θ_2 represent two critical angles between the angle ranges of wave amplification, at which the imaginary part of the wave number vanishes, and, generally, we also have the relation $\theta_2 = \theta_1 + \pi$. Here, we assume that $\theta_1 < \theta_2$, indicating that the waves will always be amplified when propagating within the range of angles from θ_1 to θ_2. However, when the magnitudes of the two odd parameters are not equal, it seems there is no symmetry for the iso-frequency contour, see Fig. 4(a) and (c), and the corresponding central angles should not exist.

From Fig. 4, we find that the wave amplification direction is mainly limited to the lower left corner or the wave attenuation direction is mainly limited to the upper right corner for the positive odd parameters. However, by changing the signs of the odd parameters, the wave amplification directions can be easily shifted to other directions, as shown in Fig. 5. For instance, for the two nonzero odd parameters with the same magnitudes, if $\bar{P}_{xx}$ is negative and $\bar{P}_{yy}$ is positive, θ_d and θ_a vary between $[\pi/2, \pi]$ and $[3\pi/2, 2\pi]$, respectively. If $\bar{P}_{xx}$ is positive and $\bar{P}_{yy}$ is negative, they vary between $[3\pi/2, 2\pi]$ and $[\pi/2, \pi]$. In the case where both odd parameters are negative, θ_d and θ_a vary between $[\pi, 3\pi/2]$ and $[0, \pi/2]$, respectively. Note that these conclusions hold not only for odd plates with bending-shear couplings along the same direction but also for other cases, such as odd plates with cross bending-shear couplings.

In Figs. 3 and 4, the qualitative tunability of the amplification directions of flexural waves in odd plates has been investigated. However, it is of fundamental importance to find a thorough approach to quantitatively characterize the control of flexural wave amplification direction by varying the odd parameters. Here, a regulation method involving the rotation of the original coordinate system, as shown in Fig. 6, is proposed to evaluate the flexural wave amplification directions. The key idea is to rotate the x-axis to coincide with the central angle of wave attenuation (opposite to the central angle of wave amplification). So the y'-axis should coincide with the critical angle θ_1-direction in view of Eq. (17). According to our previous definition, the wave number should be real for the flexural waves propagating along the critical angle θ_1 in the rotated coordinate system, which can be mathematically represented by $k_{x'} = 0$ and $\mathrm{Im}(k_{y'}) = 0$. Thus, the present problem turns into finding the relations between odd parameters to satisfy this condition in the rotated coordinate system.

To perform the coordinate system rotation, we need to transform the submatrix of odd parameters while keeping the stiffness matrix unchanged, as the material properties should remain the same after the rotation. This transformation can be expressed from Eq. (9) as

$$\mathbf{T} = \begin{bmatrix} P_{xx} & P_{yx} & 0 \\ P_{xy} & P_{yy} & 0 \end{bmatrix}. \tag{18}$$

Eqs. (4) and (5) can be rewritten in a matrix form as

$$\mathbf{Q} = \mathbf{G}\boldsymbol{\gamma} + \mathbf{TB}, \tag{19}$$

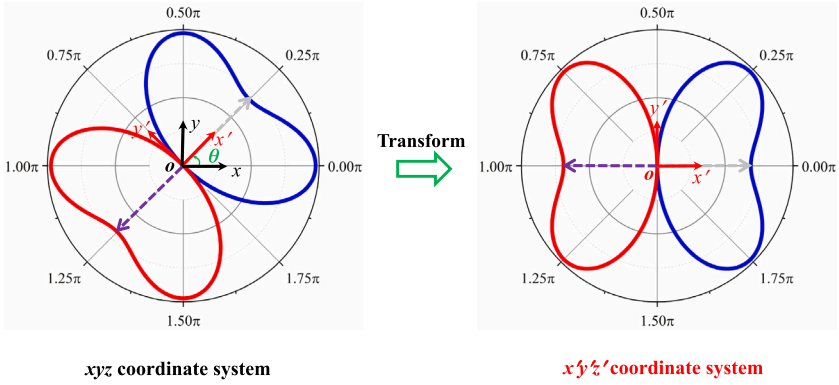

Fig. 6. Rotation of the coordinate system and the transformation of the iso-frequency contours for the imaginary part of wave number in the new rotated coordinate system.

where $\mathbf{Q} = \begin{bmatrix} Q_x & Q_y \end{bmatrix}^T$, $\boldsymbol{\gamma} = \begin{bmatrix} \gamma_{xz} & \gamma_{yz} \end{bmatrix}^T$, $\mathbf{B} = \begin{bmatrix} B_x & B_y & B_{xy} \end{bmatrix}^T$, and $\mathbf{G}$ is the shear stiffness matrix. When the coordinate system is rotated by an angle θ counterclockwise about the z-axis, the vectors of bending curvature and shear force can be represented in the new rotated coordinate system as

$$\mathbf{B}' = \mathbf{R}_B \mathbf{B}, \tag{20}$$

and

$$\mathbf{Q}' = \mathbf{R}_Q \mathbf{Q}, \tag{21}$$

where

$$\mathbf{R}_B = \begin{pmatrix} \cos^2\theta & \sin^2\theta & \cos\theta\sin\theta \\ \sin^2\theta & \cos^2\theta & -\cos\theta\sin\theta \\ -2\cos\theta\sin\theta & 2\cos\theta\sin\theta & \cos^2\theta - \sin^2\theta \end{pmatrix}, \tag{22}$$

$$\mathbf{R}_Q = \begin{pmatrix} \cos\theta & \sin\theta \\ -\sin\theta & \cos\theta \end{pmatrix}. \tag{23}$$

Based upon Eqs. (20) and (21), Eq. (19) can be rewritten in the new coordinate system as

$$\mathbf{Q}' = \mathbf{G}\boldsymbol{\gamma}' + \mathbf{T}'\mathbf{B}', \tag{24}$$

where

$$\mathbf{T}' = \mathbf{R}_Q \mathbf{T} \mathbf{R}_B^{-1}, \tag{25}$$

and $\mathbf{Q}' = \begin{bmatrix} Q_{x'} & Q_{y'} \end{bmatrix}^T$, $\gamma' = \begin{bmatrix} \gamma_{x'z'} & \gamma_{y'z'} \end{bmatrix}^T$, and $\mathbf{B}' = \begin{bmatrix} B_{x'} & B_{y'} & B_{x'y'} \end{bmatrix}^T$ represent the corresponding physical quantities in the new coordinate system. Substituting Eqs. (22) and (23) into Eq. (25) yields

$$\mathbf{T}' = \begin{bmatrix} P_{x'x'} & P_{y'x'} & P_{(x'y')x'} \\ P_{x'y'} & P_{yy'} & P_{(x'y')y'} \end{bmatrix}, \tag{26}$$

where the odd parameters in the new coordinate system read

$$P_{x'x'} = \left(P_{xx}\cos^2\theta + P_{yx}\sin^2\theta\right)\cos\theta + \left(P_{xy}\cos^2\theta + P_{yy}\sin^2\theta\right)\sin\theta, \tag{27}$$

$$P_{y'x'} = \left(P_{xx}\sin^2\theta + P_{yx}\cos^2\theta\right)\cos\theta + \left(P_{xy}\sin^2\theta + P_{yy}\cos^2\theta\right)\sin\theta, \tag{28}$$

$$P_{(x'y')x'} = \left[\left(P_{yx} - P_{xx}\right)\cos\theta + \left(P_{yy} - P_{xy}\right)\sin\theta\right]\sin\theta\cos\theta, \tag{29}$$

$$P_{x'y'} = -\left(P_{xx}\cos^2\theta + P_{yx}\sin^2\theta\right)\sin\theta + \left(P_{xy}\cos^2\theta + P_{yy}\sin^2\theta\right)\cos\theta, \tag{30}$$

$$P_{y'y'} = -\left(P_{xx}\sin^2\theta + P_{yx}\cos^2\theta\right)\sin\theta + \left(P_{yy}\cos 2\theta + P_{xy}\sin^2\theta\right)\cos\theta, \tag{31}$$

$$P_{(x'y')y'} = \left[\left(P_{xx} - P_{yx}\right)\sin\theta - \left(P_{xy} - P_{yy}\right)\cos\theta\right]\sin\theta\cos\theta. \tag{32}$$

Thus, in the new coordinate system, the constitutive relation of the odd plate can be transformed into

$$\begin{pmatrix} M_{x'} \\ M_{y'} \\ M_{x'y'} \\ Q_{x'} \\ Q_{y'} \end{pmatrix} = \begin{pmatrix} D_{11} & D_{12} & 0 & 0 & 0 \\ D_{12} & D_{11} & 0 & 0 & 0 \\ 0 & 0 & D_{33} & 0 & 0 \\ P_{x'x'} & P_{y'x'} & P_{(x'y')x'} & G & 0 \\ P_{x'y'} & P_{y'y'} & P_{(x'y')y'} & 0 & G \end{pmatrix} \begin{pmatrix} B_{x'} \\ B_{y'} \\ B_{x'y'} \\ B_{x'z'} \\ B_{y'z'} \end{pmatrix}, \tag{33}$$

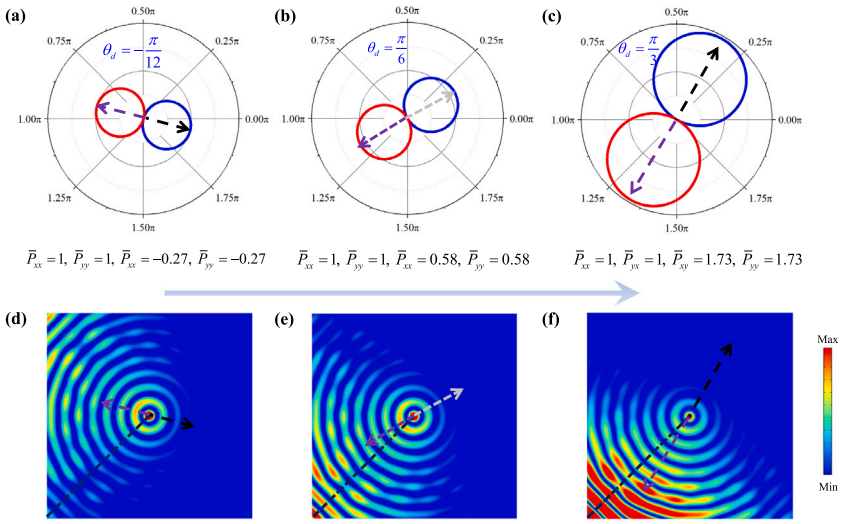

Fig. 7. Accurate control of the wave amplification directions for flexural waves in odd plates. (a–c) The iso-frequency contours for the imaginary parts of wave number. (d–f) Corresponding simulations for directional amplification of flexural waves in the considered scenarios.

where the odd parameters $P_{(x'y')x'}$ and $P_{(x'y')y'}$ represent the twist–shear couplings.

Based on the new constitutive relation of the odd plate, the dispersion relation for the flexural waves in the rotated coordinate system can be obtained. It can be easily found that the dispersion equation will be changed from the complex equation to the real equation for $k_{x'} = 0$ when the following conditions are satisfied

$$P_{x'y'} = P_{y'y'} = P_{(x'y')x'} = 0. \tag{34}$$

If there exist solutions of Eq. (34), the central angle of the wave attenuation or the wave amplification should exist, which equal to the rotation angle θ and $\theta + \pi$, respectively. For example, if the nonzero odd parameters of the odd plate are $\bar{P}_{xx} = \bar{P}_{yy} = 1.96$ in the original xyz coordinate system, the rotation angle $\theta = \theta_d = \pi/4$ satisfies Eq. (34). In the new coordinate system, the other three odd parameters are calculated as $\bar{P}_{x'x'} = \bar{P}_{y'x'} = \bar{P}_{(x'y')y'} = \bar{P}_{xx}/\sqrt{2}$ for this case, where $\bar{P}_{(x'y')y'}$ is the dimensionless form of $P_{(x'y)y'}$. The transformed iso-frequency contour in the new coordinate system exhibits the exact same shape as the iso-frequency contour in the original coordinate system, see Fig. 6. Thus, it is necessary to find a general solution to Eq. (34) to rotate the wave amplification-attenuation profile without changing the shape. In view of Eqs. (29)–(31), one solution to Eq. (34) can be achieved as

$$P_{xx} = P_{yx}, P_{yy} = P_{xy}, P_{yy} = P_{xx} \tan\theta. \tag{35}$$

Therefore, the accurate control over the flexural wave amplification direction is possible by using Eq. (35). Three examples demonstrating this control are shown in Fig. 7(a–c), where the central angle of wave attenuation θ_d is tuned from $-\pi/12$ to $\pi/3$ based on Eq. (35). By changing the signs of the odd parameters, the wave amplification direction can be shifted between different coordinate system quadrants, as shown in Fig. 5. This means that flexural waves propagating in odd plates can be theoretically controlled to amplify or attenuate in any desired direction with high accuracy.

In Fig. 8, simulation results for the active lattice plates of odd elasticity are presented to further demonstrate the effectiveness of the regulation method described by Eq. (35). It is clearly demonstrated that the proposed method is capable to control the amplification directions of flexural waves in the active lattice plates with real microstructures. In the simulation, the transfer functions should be properly designed as $H_{xx} = H_{yx}$, $H_{yy} = H_{xy}$, and $H_{yy} = H_{xx} \tan\theta_d$, where θ_d represents the central angle of wave attenuation in the lattice as $-\pi/12$, $\pi/6$, $\pi/3$, $3\pi/4$, $-3\pi/4$, and $-\pi/4$ in Fig. 8(a–g), respectively. The transfer function H_{xx} is selected to be 6 in Fig. 8(a–c) and (f) and -6 in Fig. 8(d) and (e). The lattice plate consists of 8×8 unit cells whose material and geometric parameters are listed in Tables 1 and 2, respectively, and PMLs are implemented at the boundaries to reduce reflections.

To validate the effectiveness of the plate theory in modeling wave propagation in the active lattice, we present simulations of waves propagating in the effective odd plates, as depicted in Fig. 9. For quantitative comparisons, the contour plots display displacement field magnitudes using the same scale employed in Fig. 8, which illustrates wave propagation in the active lattices. The remarkable consistency between Figs. 8 and 9 is apparent, confirming the applicability of the effective plate theory for the study of wave propagation within the active lattices. Furthermore, in order to further examine the validation of the effective theory, Fig. C.1 provides quantitative comparisons of wave amplitudes along the dotted circles in both the effective plates and the active lattices, as presented in Appendix C.

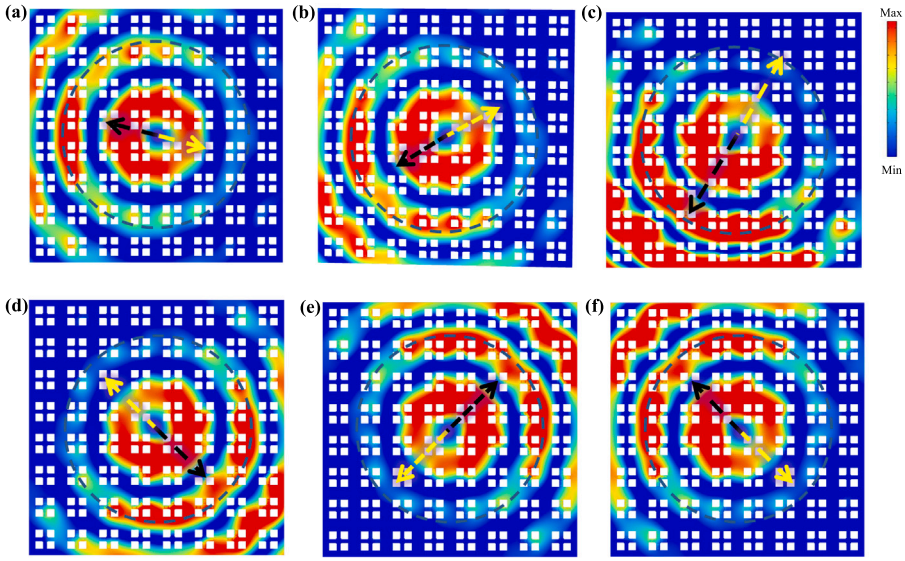

Fig. 8. Control of the amplification-attenuation directions for flexural waves propagating in the active lattice plate of odd elasticity. (a–f) Numerically obtained flexural wave field distributions with θ_d selected as (a) $-\pi/12$, (b) $\pi/6$, (c) $\pi/3$, (d) $3\pi/4$, (e) $-3\pi/4$, and (f) $-\pi/4$. The black arrows represent the central angle of wave amplification, while the yellow arrows represent the central angle of wave attenuation. The excitation source is placed at the center of the lattice plate, and the excitation frequency is set to 1000 Hz. The lattice plate consists of 8×8 unit cells, and PMLs are implemented at the boundaries to reduce reflection. The dashed circles are used to measure azimuthal wave amplitudes at the radius of 0.15 m for quantitative comparisons illustrated in Fig. C.1 in Appendix C.

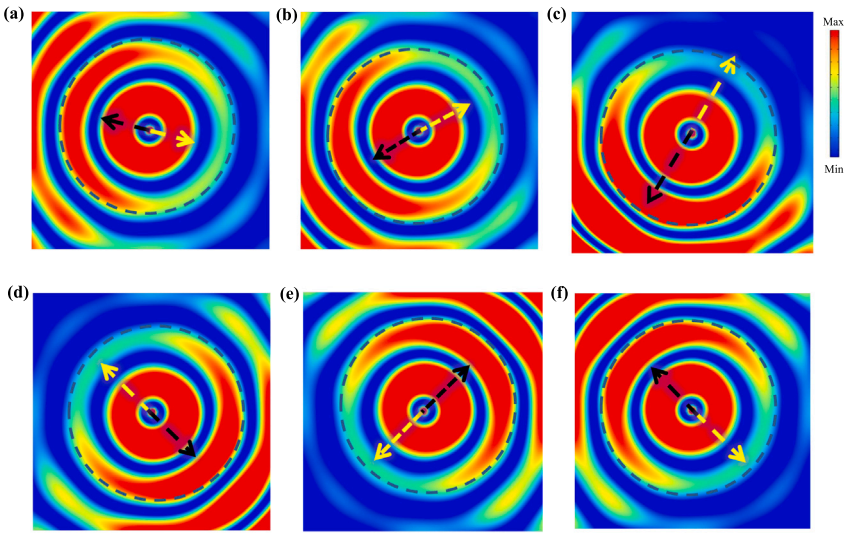

Fig. 9. Wave fields in effective odd plates corresponding to the cases illustrated in Fig. 8.

4. Stoneley-like interfacial waves between two odd plates

In this section, we will explore the underlying physical mechanisms that Stoneley-like interfacial waves can exist between two adjacent odd plates, characterize propagation properties of these waves, and also illustrate their intriguing properties in terms of confinement, and reconfigurability. The interface is constructed at the location $x = 0$, where the two odd plates meet, as schematically shown in Fig. 10. We introduce a new form of interfacial waves that can be sustained at a planar interface-impedance discontinuity characterized by the two odd parameters with opposite signs as

$$-P^l_{xx} = P^r_{xx} = P_{xx}, \quad -P^l_{yx} = P^r_{yx} = P_{yx}, \tag{36}$$

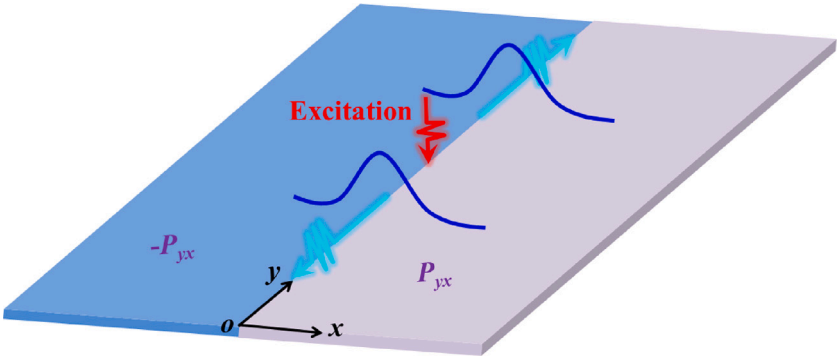

Fig. 10. Conceptual diagram illustrating flexural waves propagating along the interface between odd plates. The two odd plates have the same material properties but differ only in their odd parameters.

where the superscripts "l" and "r" indicate the regions lying on the left ($x < 0$) and right ($x > 0$) sides of the interface. The displacement fields for flexural waves can be expressed as

$$w^l = W^l e^{ik_x^l x} e^{i(k_y y - \omega t)}, \psi_x^l = \Psi_x^l e^{ik_x^l x} e^{i(k_y y - \omega t)}, \psi_y^l = \Psi_y^l e^{ik_x^l x} e^{i(k_y y - \omega t)} \tag{37}$$

in the region $x < 0$, and

$$w^r = W^r e^{ik_x^r x} e^{i(k_y y - \omega t)}, \psi_x^r = \Psi_x^r e^{ik_x^r x} e^{i(k_y y - \omega t)}, \psi_y^r = \Psi_y^r e^{ik_x^r x} e^{i(k_y y - \omega t)} \tag{38}$$

in the region $x > 0$. Similar to the conventional Stoneley waves, the interfacial waves should exist if we could identify the interfacial waves that propagate along the interface with constant amplitudes and exponentially decay away from the interface. Mathematically, the wave numbers must satisfy conditions

$$\mathrm{Re}\left(k_y\right) \neq 0, \quad \mathrm{Im}\left(k_y\right) = 0 \tag{39}$$

$$\mathrm{Im}\left(k_x\right) < 0, \quad x < 0 \tag{40}$$

$$\mathrm{Im}\left(k_x\right) > 0, \quad x > 0 \tag{41}$$

Without loss of generality, we assume

$$k_x^l = -id^l, \quad k_x^r = id^r, \tag{42}$$

where both of d^l and d^r are assumed to be real and positive. It is important to emphasize that the conditions $P_{xy}^l = P_{xy}^r = 0$ and $P_{yy}^l = P_{yy}^r = 0$ are crucial for satisfying the condition described by Eq. (39). By substituting the two expressions from Eq. (42) into Eq. (15) separately, we can derive two dispersion equations, each corresponding to one of the odd plates. Remarkably, both equations feature real coefficients. Additionally, in view of Eq. (36), we find that the two dispersion equations for the odd plates become identical when we set

$$d^l = d^r = d \quad (d > 0). \tag{43}$$

Thus, the displacement fields on both sides of the interface can be specified as, for $x > 0$,

$$\begin{aligned} w^r &= h\left(A_1 e^{-d_1 x} + A_2 e^{-d_2 x} + A_3 e^{-d_3 x}\right) e^{i(k_y y - \omega t)}, \\ \psi_x^r &= \left(\beta_x^1 A_1 e^{-d_1 x} + \beta_x^2 A_2 e^{-d_2 x} + \beta_x^3 A_3 e^{-d_3 x}\right) e^{i(k_y y - \omega t)}, \\ \psi_y^r &= \left(\beta_y^1 A_1 e^{-d_1 x} + \beta_y^2 A_2 e^{-d_2 x} + \beta_y^3 A_3 e^{-d_3 x}\right) e^{i(k_y y - \omega t)}, \end{aligned} \tag{44}$$

and for $x < 0$,

$$\begin{aligned} w^l &= h\left(A_4 e^{d_1 x} + A_5 e^{d_2 x} + A_6 e^{d_3 x}\right) e^{i(k_y y - \omega t)}, \\ \psi_x^l &= -\left(\beta_x^1 A_4 e^{d_1 x} + \beta_x^2 A_5 e^{d_2 x} + \beta_x^3 A_6 e^{d_3 x}\right) e^{i(k_y y - \omega t)}, \\ \psi_y^l &= \left(\beta_y^1 A_4 e^{d_1 x} + \beta_y^2 A_5 e^{d_2 x} + \beta_y^3 A_6 e^{d_3 x}\right) e^{i(k_y y - \omega t)}, \end{aligned} \tag{45}$$

where d_1, d_2 and d_3 must be real and positive roots of the dispersion equations, $\beta_x^i = \bar{\Psi}_x / \bar{W}$ and $\beta_y^i = \bar{\Psi}_y / \bar{W}$ can be obtained for each $d_i (i = 1, 2, 3)$ by employing Eq. (15) along with Eqs. (36), (42), and (43), and $A_i (i = 1 - 6)$ are the constants. The displacement field must satisfy the interfacial conditions to ensure its continuity across the interface, which can be represented by

$$\begin{aligned} &w^r = w^l, \psi_x^r = \psi_x^l, \psi_y^r = \psi_y^l, \\ &M_x^l = M_x^r, M_{yx}^l = M_{yx}^r, Q_x^l = Q_x^r. \end{aligned} \tag{46}$$

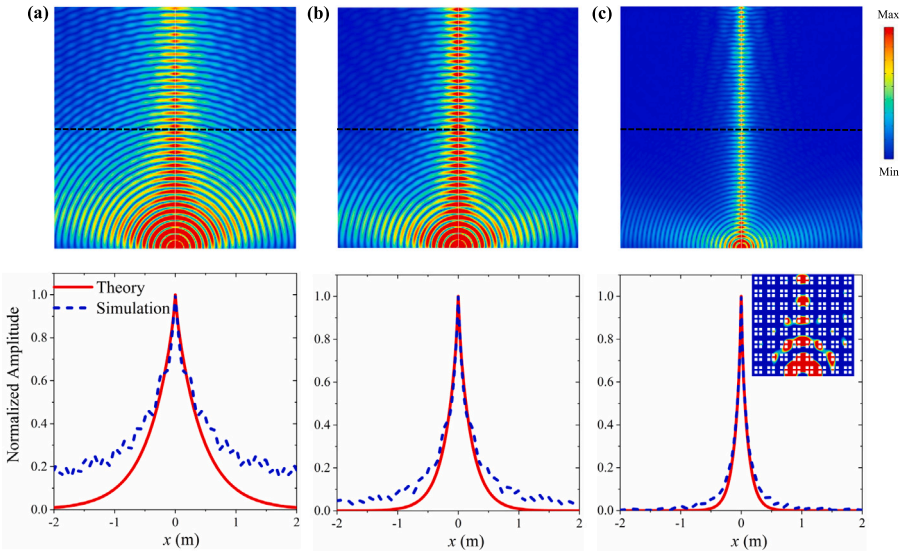

Fig. 11. Simulations of interfacial flexural waves propagating along the interface in the y-direction and their corresponding comparisons with theory for (a) $\bar{P}_{yx} = 1.96, \Omega = 0.031$, (b) $\bar{P}_{yx} = 3.92, \Omega = 0.031$, and (c) $\bar{P}_{yx} = 3.92, \Omega = 0.062$. The normalized amplitudes are measured at the dashed lines. The inset in (c) showcases the field distributions of interfacial waves in the corresponding active lattice plate.

In view of Eqs. (9), (44) and (45), the interfacial conditions given by Eq. (46) can be further simplified into

$$A_1 = A_4, A_2 = A_5, A_3 = A_6, \tag{47}$$

$$\psi_x^r = 0, M_{xy}^r = 0, Q_x^r = 0. \tag{48}$$

Thus, we only need to consider the waves on the right side of the interface with the boundary conditions given by Eq. (48), which can be specified in a matrix form as

$$\begin{bmatrix} \beta_x^1 & \beta_x^2 & \beta_x^3 \\ B_{51} & B_{52} & B_{53} \\ B_{61} & B_{62} & B_{63} \end{bmatrix} \begin{bmatrix} A_1 \\ A_2 \\ A_3 \end{bmatrix} = 0, \tag{49}$$

where

$$\begin{aligned} B_{51} &= d_1\beta_y^1 - ik_y\beta_x^1, B_{52} = d_2\beta_y^2 - ik_y\beta_x^2, \\ B_{53} &= d_3\beta_y^3 - ik_y\beta_x^3, \\ B_{61} &= \left(d_1 - \beta_x^1\right) + \bar{P}_{xx}d_1\beta_x^1 - \bar{P}_{yx}ik_y\beta_y^1, \\ B_{62} &= \left(d_2 - \beta_x^2\right) + \bar{P}_{xx}d_2\beta_x^2 - \bar{P}_{yx}ik_y\beta_y^2, \\ B_{63} &= \left(d_3 - \beta_x^3\right) + \bar{P}_{xx}d_3\beta_x^3 - \bar{P}_{yx}ik_y\beta_y^3. \end{aligned}$$

To obtain non-trivial solutions to Eq. (49), the determinant of the coefficient matrix must be zero, namely

$$\begin{vmatrix} \beta_x^1 & \beta_x^2 & \beta_x^3 \\ B_{51} & B_{52} & B_{53} \\ B_{61} & B_{62} & B_{63} \end{vmatrix} = 0. \tag{50}$$

If interfacial waves exist on the interface between two odd plates, both the dispersion equation [Eq. (15)] and the interfacial conditions must be satisfied, subject to the following constraints: the real value of k_y and the real and positive values of d_1, d_2, and d_3.

For the interface along the y-axis, satisfying the condition represented by Eq. (39) requires both odd parameters $\bar{P}_{xy}$ and $\bar{P}_{yy}$ to be zero. Thus, we only need to consider the remaining two cases: $\bar{P}_{xx} \neq 0$, $\bar{P}_{yx} = 0$ and $\bar{P}_{xx} = 0$, $\bar{P}_{yx} \neq 0$. However, in the first case $\left(\bar{P}_{xx} \neq 0, \bar{P}_{yx} = 0\right)$, the interface should be weak since the difference between the shear forces induced by odd elasticity on the two sides of the interface is small. This occurs because the bending deformation along the x-axis is minimal for waves propagating along the y-axis interface. On the other hand, in the second case $\left(\bar{P}_{xx} = 0, \bar{P}_{yx} \neq 0\right)$, the bending deformation remains unchanged for an interfacial wave propagating along the y-axis interface, resulting in distinct interfacial waves as observed in Fig. 11(a–c). Thus, the cross coupling between bending and shear in different directions is crucial for the formation of interfacial waves in odd plates.

To confirm that the interfacial flexural waves depicted in Fig. 11(a–c) exhibit Stoneley-like behavior, we compare the amplitudes obtained from the numerical simulation with those from the analytical solutions presented in Eqs. (44) and (45). The comparison

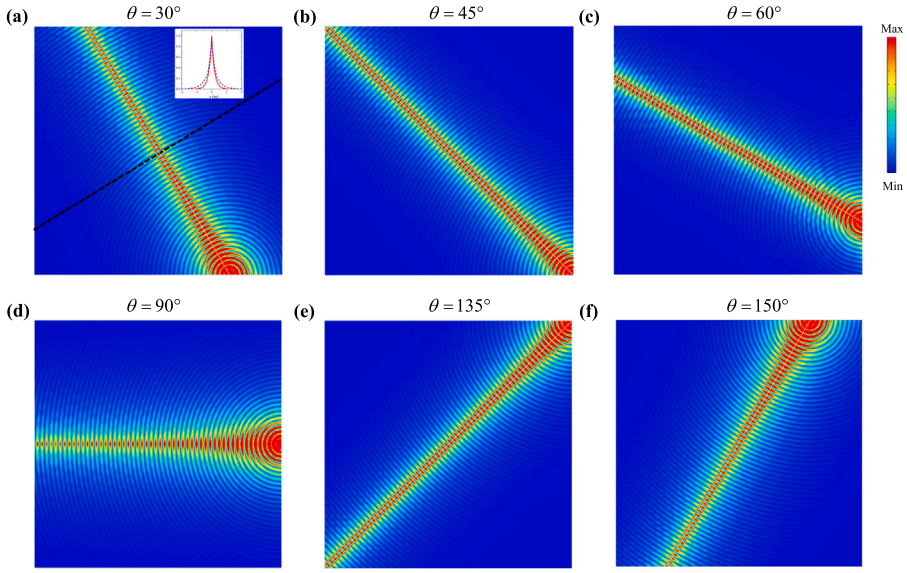

Fig. 12. Rotation of the interface in an odd plate by varying the odd parameters. (a–f) Numerically obtained flexural wave field distributions with the normal direction of the interface being selected as (a) 30°, (b) 45°, (c) 60°, (d) 90°, (e) 135°, and (f) 150°. The dimensionless excitation frequency is 0.062. The inserted figure in (a) shows the comparison of the displacement field distributions along the dotted line obtained from the simulation and the corresponding analytical solution.

reveals good agreement between the two results in the regions near the interface and away from the excitation source. Discrepancies between the two curves can be attributed to the interference of bulk waves in the simulation results. Bulk waves diminish significantly in regions distant from the point excitation source due to scattering effects. In contrast, interfacial waves propagate with constant amplitudes. This particular attribute presents a noteworthy benefit of the interfacial waves by facilitating concentrated wave energy along the interface. It is worth noting that increasing the frequency and magnitude of the odd parameter enhances the energy concentration on the interface. This is evident from the comparison between Fig. 11(a) and (b) for the different odd parameters, as well as the comparison between Fig. 11(b) and (c) for the different excitation frequencies. Unlike the interfacial waves in topological structures (Chen et al., 2018) and chiral structures (Carta et al., 2020), the interfacial waves between odd plates have no limitations on working frequency. It should be noted that the odd parameter on the right side of the interface must be positive to satisfy the condition of having real and positive values for d_1, d_2, and d_3. Consequently, the odd parameter on the left side of the interface should be negative. The interfacial waves also exist in the odd plate through the appropriate arrangement of the transfer functions, see the inserted figure in Fig. 11 for example.

In order to enhance design flexibility and wave reconfigurability, a proposition is made to create an interface in any desired direction. The key aspect involves determining the odd parameters on both sides of the interface. To accomplish this, the technique of coordinate system rotation is utilized by aligning the y-axis with the interface. As a result, the relationship between the four parameters can be established using Eq. (35). In Fig. 12, it is demonstrated that the interface between odd plates can be continuously rotated by simply adjusting the odd parameters. The odd parameters $\left(\bar{P}xx \text{ and } \bar{P}yy\right)$ on the right-hand side of the interface in Fig. 12 are chosen as: (a) $(1.96, 1.13)$, $(b)(1.96, 1.96)$, (c) $(1.57, 2.72)$, (d) $(0, 1.96)$, (e)$(-1.96, 1.96)$, (f) $(-1.96, 1.13)$. It should be noted that the odd parameters must also satisfy $\bar{P}_{yx} = \bar{P}_{xx}$ and $\bar{P}_{xy} = \bar{P}_{yy}$.

Considering the ability of the Stonley-like interfacial waves to effectively trap energy at the interface, the assembly of odd plates holds promise for designing exceptional waveguides. Taking advantage of this, we demonstrate the design of multichannel waveguides with distinct shapes by assembling different units of triangular odd plates using the method described earlier. In Fig. 13, we present the examples of different shaped waveguides. It should be noted that the variations among the triangular odd plate units lie solely in the odd parameters, with each unit satisfying $\bar{P}_{yx} = \bar{P}_{xx} = N_x$ and $\bar{P}_{xy} = \bar{P}_{yy} = N_y$. The different odd plate units, identified as (1–8) in Fig. 13, correspond to distinct odd parameters $\left(N_x, N_y\right)$. Theoretically, waveguides of any desired shape can be realized as long as the plate is sufficiently large, given the capability of forming interfaces between odd plates along arbitrary directions.

It is necessary to note that the interfacial wave studied in this section is a distinct wave solution, primarily satisfying the interfacial continuity condition between two odd plates. It behaves akin to conventional Rayleigh waves on a single half-space or Stoneley waves occurring between two neighboring half-spaces in a conventional medium. While the wave propagation phenomenon shows similarities to that of the topological interfacial wave, the underlying mechanism for realizing the interfacial wave in the odd plate is fundamentally distinct from that of the topological interfacial wave, which is typically caused by breaking time or space symmetry (Chen et al., 2018, 2019). As a result, the topological interfacial wave is confined to the bandgap frequency range, whereas the interfacial wave phenomena in the odd plate are not bound by this limitation and can take place across a broader frequency

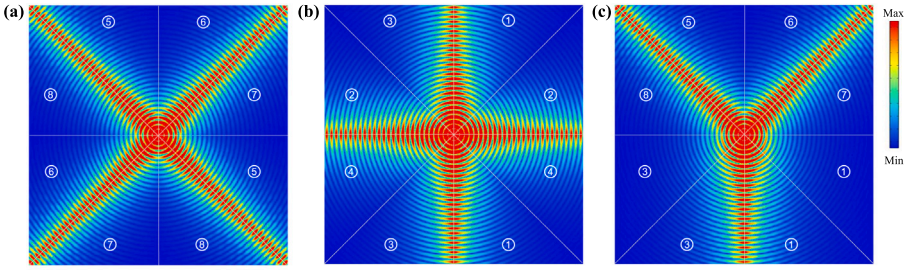

Fig. 13. Multi-channel waveguides assembled by triangular odd plates. (a–c) Numerically obtained flexural wave field distributions with "X"-, "+"- and "Y"-shaped waveguides. The indexed triangular odd plates have different odd parameters (N_x, N_y), which are (1)$(\bar{P}, 0)$, (2)$(0, \bar{P})$, (3)$(-\bar{P}, 0)$, (4)$(0, -\bar{P})$, (5)$(\bar{P}, \bar{P})$, (6)$(-\bar{P}, \bar{P})$, (7)$(\bar{P}, -\bar{P})$, and (8)$(-\bar{P}, -\bar{P})$, where $\bar{P} = 1.96$. The interfacial waves are excited by a point source of a dimensionless frequency of 0.062 at the center.

spectrum. However, the interfacial wave in the odd plate lacks the robust property of preventing the backscattering of topological waves at lattice interfaces and boundaries, a characteristic typically quantified by topological numbers such as Chern number.

5. Conclusion

This paper primarily focuses on the microstructure design of odd plates, along with a comprehensive theoretical investigation into its wave dynamics. Initially, an active lattice plate is proposed, which incorporates a piezoelectric-patch-based sensor–actuator feed-forward system to establish a nonreciprocal coupling between bending deformation and shear forces. It is demonstrated that the active lattice plate can be homogenized as an effective odd plate, which has four odd parameters that can be adjusted independently. The performance of the proposed odd plate theory is validated against the active exact model through the comparison of the iso-frequency contour prediction. Under the framework of the odd plate, we demonstrate that the flexural wave amplification directions could be controllable via the tune of the odd parameters. A thorough approach for precise wave control is further analytically derived by using the rotation of the coordinate system, which can also serve as a valuable guide for the control of flexural waves in active lattice plate of odd elasticity. In addition, we theoretically uncover the existence of the Stoneley-like interfacial waves between odd plates with the odd parameters of opposite signs. We illustrate numerically the propagation properties of these waves and the underlying physical mechanisms and also quantitatively investigate their intriguing properties in terms of confinement and reconfigurability. Finally, we address possible practical implementations based on odd pates. Our results hold intriguing potentials for applications in extreme waveguiding and reconfigurable wave steering in the plate, potentially paving the way for further research on 2D non-Hermitian systems in elasticity.

CRediT authorship contribution statement

Yanzheng Wang: Conceptualization, Formal analysis, Performing simulations, Validation, Writing. **Qian Wu:** Formal analysis, Performing simulations, Writing. **Yiran Tian:** Performing simulations. **Guoliang Huang:** Conceptualization, Supervision, Validation, Funding acquisition, Writing.

Declaration of competing interest

The authors declare that they have no known competing financial interests or personal relationships that could have appeared to influence the work reported in this paper.

Data availability

Data will be made available on request.

Acknowledgments

This work is supported by the Air Force Office of Scientific Research, United States under Grant No. AF 9550-18-1-0342 and AF 9550-20-1-0279 with Program Manager Dr. Byung-Lip (Les) Lee.

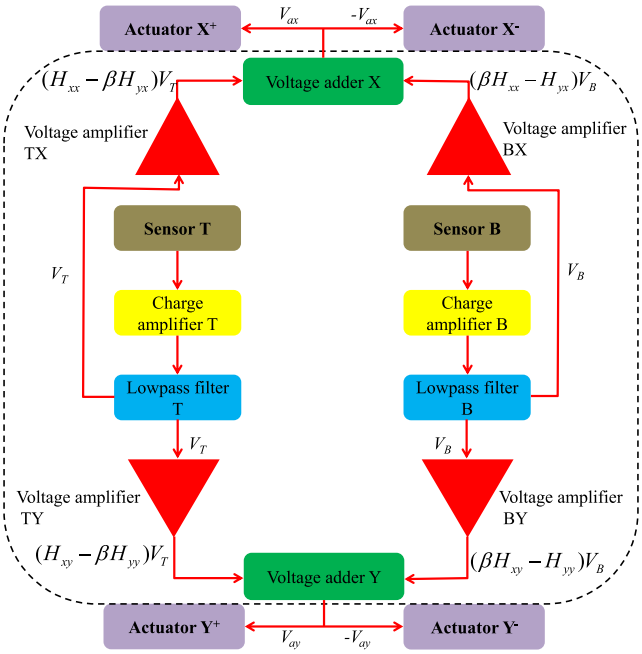

Fig. A.1. Schematic of the digital control system. In this diagram, "T" and "B" correspond to the electronic devices associated with the sensors located on the top and bottom, respectively. Similarly, "X" and "Y" represent the electronic devices connected to the actuators along the x-axis and y-axis, respectively. Additionally, the superscripts "+" and "−" indicate the actuators affixed to the positive and negative directions of either the x-axis or the y-axis.

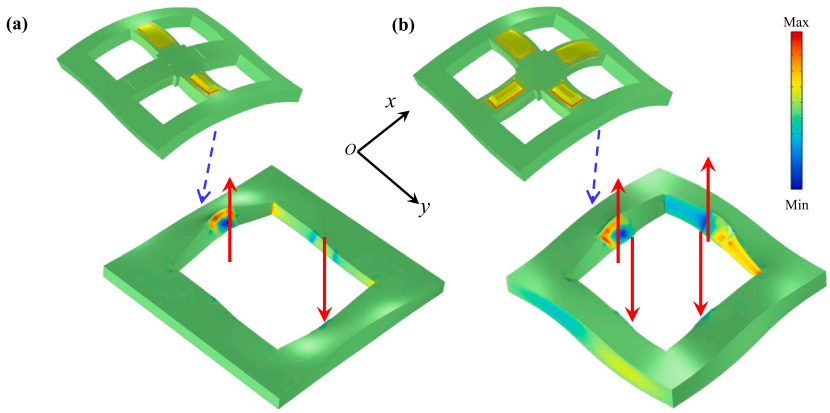

Fig. B.1. Static shear deformations induced by the active beams: (a) Unit cell with a single active beam in the y-direction, (b) Unit cell with an active beam in the x-direction and another active beam in the y-direction. The arrow lines indicate the directions of shear forces generated by the active beams on the frame.

Appendix A. Schematic of digital control system

The schematic diagram of the digital control system is depicted in Fig. A.1. This system comprises two charge amplifiers, two frequency-dependent lowpass filters, and four voltage amplifiers. These components are employed to extract electric charges from the surfaces of piezoelectric sensing patches located both on the top and bottom of the beams. The charge amplifiers extract these charges, while the frequency-dependent lowpass filters play a crucial role in filtering out noise signals originating from the surrounding environment. Subsequently, the sensing voltages, denoted as V_T and V_B, undergo amplification through the voltage amplifiers. By utilizing voltage adders and transfer functions, the resulting output voltages ($\pm V_{ax}$ and $\pm V_{ay}$) are differentially applied to two sets of actuators situated along the x-axis and y-axis, respectively. For the current design, the relationship between the sensor voltages and the actuator voltages can be expressed as $V_{ax} = (H_{xx} - \beta H_{yx})V_T + (\beta H_{xx} - H_{yx})V_B$ and $V_{ay} = (H_{xy} - \beta H_{yy})V_T + (\beta H_{xy} - H_{yy})V_B$. These equations are derived from Eqs. (2) and (3).

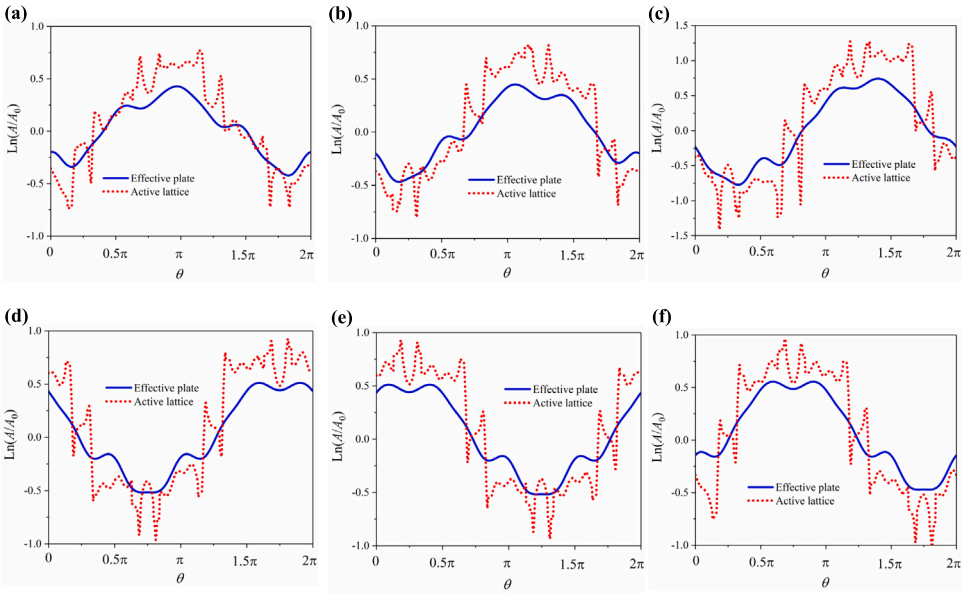

Fig. C.1. Quantitative comparisons of wave amplitudes along dotted circles in actual lattices and effective plates, with a propagation radius of 0.15 m.

Appendix B. The shear deformations induced by the active beams

Fig. B.1 illustrates the static shear deformations of the unit cell within the active lattice. These deformations result from the activation of the beams, achieved by applying antisymmetric voltages to a pair of actuators.

Appendix C. Comparisons of the wave amplitudes

Fig. C.1 presents quantitative comparisons of wave amplitudes for waves propagating within the actual lattices and the effective plates. The data points are extracted from Figs. 8 and 9, respectively, along the dotted circles. The radii of all the circles are consistent at 0.15 m. Within this context, A_0 represents the amplitude at angles of 0.25π or 1.25π, where the waves remain unaffected by amplification or attenuation.

References

Bahaloo, H., Li, Y., 2019. Micropolar modeling of auxetic chiral lattices with tunable internal rotation. J. Appl. Mech. 86 (4).
Binysh, J., Souslov, A., 2022. Odd living matter defies the golden rule of mechanics.
Brandenbourger, M., Locsin, X., Lerner, E., Coulais, C., 2019. Non-reciprocal robotic metamaterials. Nat. Commun. 10 (1), 4608.
Brandenbourger, M., Scheibner, C., Veenstra, J., Vitelli, V., Coulais, C., 2021. Limit cycles turn active matter into robots. arXiv preprint arXiv:2108.08837.
Carta, G., Colquitt, D., Movchan, A., Movchan, N., Jones, I., 2020. Chiral flexural waves in structured plates: directional localisation and control. J. Mech. Phys. Solids 137, 103866.
Chen, Y., Li, X., Scheibner, C., Vitelli, V., Huang, G., 2021. Realization of active metamaterials with odd micropolar elasticity. Nat. Commun. 12 (1), 5935.
Chen, H., Nassar, H., Huang, G., 2018. A study of topological effects in 1D and 2D mechanical lattices. J. Mech. Phys. Solids 117, 22–36.
Chen, H., Yao, L., Nassar, H., Huang, G., 2019. Mechanical quantum hall effect in time-modulated elastic materials. Phys. Rev. A 11 (4), 044029.
Cheng, W., Hu, G., 2021. Odd elasticity realized by piezoelectric material with linear feedback. Sci. China Phys. Mech. Astron. 64 (11), 2.
Domínguez-Rocha, V., Thevamaran, R., Ellis, F., Kottos, T., 2020. Environmentally induced exceptional points in elastodynamics. Phys. Rev. A 13 (1), 014060.
El-Ganainy, R., Makris, K.G., Khajavikhan, M., Musslimani, Z.H., Rotter, S., Christodoulides, D.N., 2018. Non-Hermitian physics and PT symmetry. Nat. Phys. 14 (1), 11–19.
Fruchart, M., Scheibner, C., Vitelli, V., 2023. Odd viscosity and odd elasticity. Annu. Rev. Condens. Matter Phys. 14, 471–510.
Gao, P., Qu, Y., Christensen, J., 2022. Non-Hermitian elastodynamics in gyro-odd continuum media. Commun. Mater. 3 (1), 74.
Gu, Z., Gao, H., Xue, H., Li, J., Su, Z., Zhu, J., 2022. Transient non-Hermitian skin effect. Nature Commun. 13 (1), 7668.
Gupta, A., Kurnosov, A., Kottos, T., Thevamaran, R., 2023. Reconfigurable enhancement of actuation forces by engineered losses in non-Hermitian metamaterials. Extreme Mech. Lett. 59, 101979.
Liu, X., Huang, G., Hu, G., 2012. Chiral effect in plane isotropic micropolar elasticity and its application to chiral lattices. J. Mech. Phys. Solids 60 (11), 1907–1921.
Milton, G.W., 2013. Complete characterization of the macroscopic deformations of periodic unimode metamaterials of rigid bars and pivots. J. Mech. Phys. Solids 61 (7), 1543–1560.
Milton, G.W., Willis, J.R., 2007. On modifications of Newton's second law and linear continuum elastodynamics. Proc. R. Soc. A 463 (2079), 855–880.
Moccia, M., Castaldi, G., Alu, A., Galdi, V., 2020. Line waves in non-Hermitian metasurfaces. ACS Photonics 7 (8), 2064–2072.
Nassar, H., Chen, Y., Huang, G., 2019. Isotropic polar solids for conformal transformation elasticity and cloaking. J. Mech. Phys. Solids 129, 229–243.
Nassar, H., Chen, Y., Huang, G., 2020. Polar metamaterials: a new outlook on resonance for cloaking applications. Phys. Rev. Lett. 124 (8), 084301.
Rosa, M.I., Ruzzene, M., 2020. Dynamics and topology of non-Hermitian elastic lattices with non-local feedback control interactions. New J. Phys. 22 (5), 053004.

Scheibner, C., Irvine, W.T., Vitelli, V., 2020a. Non-Hermitian band topology and skin modes in active elastic media. Phys. Rev. Lett. 125 (11), 118001.
Scheibner, C., Souslov, A., Banerjee, D., Surówka, P., Irvine, W.T., Vitelli, V., 2020b. Odd elasticity. Nat. Phys. 16 (4), 475–480.
Shaat, M., Park, H.S., 2023. Chiral nonreciprocal elasticity and mechanical activity. J. Mech. Phys. Solids 171, 105163.
Tan, T.H., Mietke, A., Li, J., Chen, Y., Higinbotham, H., Foster, P.J., Gokhale, S., Dunkel, J., Fakhri, N., 2022. Odd dynamics of living chiral crystals. Nature 607 (7918), 287–293.
Wang, W., Wang, X., Ma, G., 2022. Non-Hermitian morphing of topological modes. Nature 608 (7921), 50–55.
Wu, Q., Chen, Y., Huang, G., 2019. Asymmetric scattering of flexural waves in a parity-time symmetric metamaterial beam. J. Acoust. Soc. Am. 146 (1), 850–862.
Wu, Q., Shivashankar, P., Xu, X., Chen, Y., Huang, G., 2023a. Engineering nonreciprocal wave dispersion in a nonlocal micropolar metabeam. J. Compos. Mater. 57 (4), 771–782.
Wu, Q., Xu, X., Qian, H., Wang, S., Zhu, R., Yan, Z., Ma, H., Chen, Y., Huang, G., 2023b. Active metamaterials for realizing odd mass density. Proc. Natl. Acad. Sci. 120 (21), e2209829120.
Wu, Q., Zhang, X., Shivashankar, P., Chen, Y., Huang, G., 2022. Independent flexural wave frequency conversion by a linear active metalayer. Phys. Rev. Lett. 128 (24), 244301.
Xue, H., Yang, Y., Zhang, B., 2022. Topological acoustics. Nat. Rev. Mater. 1–17.
Yi, J., Ma, Z., Xia, R., Negahban, M., Chen, C., Li, Z., 2022. Structural periodicity dependent scattering behavior in parity-time symmetric elastic metamaterials. Phys. Rev. B 106 (1), 014303.
Zhang, X., Zhang, T., Lu, M.-H., Chen, Y.-F., 2022. A review on non-Hermitian skin effect. Adv. Phys.: X 7 (1), 2109431.